

# Investigation of unsteady cavitating flow around a hydrofoil using GAS method

## Original article

### Article history:

Submission date: 29 November 2023

Acceptance date: 4 May 2024

Publication date: 30 July 2024

This is the updated version of a paper originally presented at the Global Power and Propulsion Technical Conference, GPPS Hong Kong23, October 17-19, 2023.



### \*Correspondence:

YL: liuyangwei@126.com

### Peer review:

Single blind

### Copyright:

© 2024 Xie et al. © This is an open access article distributed under the Creative Commons Attribution Non Commercial No Derivatives License (CC BY-NC-ND 4.0). Unrestricted use, distribution, and reproduction of the original work are permitted for noncommercial purposes only, provided it is properly cited and its authors credited. No derivative of this work may be distributed.

### Keywords:

cavitating flow; hydrofoil; grid-adaptive simulation; tip leakage vortex

### Citation:

Xie N., Tang Y., Hou J., and Liu Y. (2024). Investigation of unsteady cavitating flow around a hydrofoil using GAS method. *Journal of the Global Power and Propulsion Society*, 8: 255–268.  
<https://doi.org/10.33737/jgpps/188263>

Nan Xie<sup>1,2</sup>, Yumeng Tang<sup>1,2</sup>, Jiexuan Hou<sup>1,2</sup>, Yangwei Liu<sup>1,2,\*</sup>

<sup>1</sup>School of Energy and Power Engineering, Beihang University No.37 Xueyuan Road, Haidian District, Beijing 100191, China

<sup>2</sup>National Key Laboratory of Science and Technology on Aero-Engine Aero-Thermodynamics, Beihang University No.37 Xueyuan Road, Haidian District, Beijing 100191, China

## Abstract

Cavitation significantly impacts the performance of hydraulic machinery. However, cavitation is complex, and the evolution of complex vortical structures in cavitating flow requires further investigation. In this study, the unsteady cavitating flow around a NACA0009 hydrofoil with gap sizes of 1 and 10 mm is simulated using grid-adaptive simulation (GAS), which is a novel hybrid method that modifies the turbulent viscosity based on the Kolmogorov energy spectrum. The prediction accuracy of GAS is validated by comparing with experimental and LES results, demonstrating its superiority compared to the scale-adaptive simulation. A detailed study on the effect of gap size with an emphasis on the evolution of complex vortical structures is performed. It is discovered that the gap size plays a crucial role in the development of complex flow structures, as well as their interactions. Moreover, as the gap size increases, the two-layer structure of tip leakage vortex (TLV) becomes more pronounced. The inner TLV core region is generated by the vorticity transport from tip to the TLV. The outer layer structure is formed by the mainstream, tip separation vortex and leakage flow. The complex outer layer significantly influences the stability of the TLV and cavities. The investigation on the TLV structure in this study of cavitation flow aligns with the previous conclusions in compressors, indicating that two-layer structure of the TLV is a universal phenomenon.

## Introduction

Cavitation has received a sustained attention since it was firstly discovered in the 19th century (Zhang et al., 2015). Typically, the cavitation in hydraulic machinery typically causes serious damages, such as fatigue and erosion (Huang et al., 2019; Peng et al., 2019). Although many studies have been conducted over decades to reveal its fundamental mechanism, cavitation remains a challenge in the design of hydraulic machinery. Generally speaking, the gap between the blade tip and the shroud is prevalent in the axial and centrifugal pumps. Since the pressure difference between the pressure side (PS) and the suction side (SS) of the blade, the fluid near the blade tip moves from the PS to the SS through the gap, resulting in complex vortical structures, such as tip leakage vortex (TLV), induced vortex (IV) and tip separation vortex (TSV). When the strength of vortical structures is strong enough, the pressure in the vortex core regions drops below the saturated vapor pressure, and the vortex cavitation occurs.

Among the factors that affect vortical structures near the tip, the gap size is considered to be the very important. A lot of studies have been conducted to investigate the relationship between gap size and the TLV of axial compressors (Williams et al., 2010; Sakulkaew et al., 2013; Hou et al., 2022). It is observed that the vorticity transport related to blade tip and the end wall plays a major role in the evolution of vortical structures in the blade tip region, leading to key effects on stability and unsteadiness of the TLV (Hou et al., 2022; Hou and Liu, 2023). Another interesting discovery is that the TLV in axial compressors is composed of a two-layer structure. The inner TLV core region is generated by the vorticity transport from the tip shear layer to the TLV, and the outer layer is formed by the shearing between the leakage jet and the passage flow.

There are also many experimental and numerical studies with emphasis on the TLV in hydraulic machinery. The effect of gap size on the tip leakage vortex cavitation (TLVC) adds a new level of complexity to the vortical structures (Boulon et al., 1999). Farrell and Billet (1994) studied the effect of gap size on the TLVC in an axial pump and found that the cavitation inception index decreases as the gap size increase. This conclusion was subsequently confirmed by the experiments of Gopalan et al. (2002) based on a hydrofoil. Dreyer et al. (2014) and Dreyer (2015) conducted systematic experiments focusing on the effect of the gap size on the TLVC in cavitating flow around a NACA0009 hydrofoil. The existence of a specific gap size for which the TLV strength reaches its peak is revealed, and this specific gap size is closely related to the incidence angle. Base on the experiments of Dreyer et al. (2014) and Dreyer (2015), many numerical investigations are carried out to have a deeper understanding of the effect of gap size (Xu et al., 2020; Wang et al., 2023). However, many previous researches only focus on the TLVC, while other flow structures, such as leading-edge cavitation (LEC), also have a significant impact on the performance of hydraulic machinery. Unfortunately, systematic analyses of the effect of gap size in cavitating flow are still lacking.

Since the growth and collapse of the vapor bubble contains many complex characteristics, such as turbulence, compressibility, mass and heat transfer, etc., thus it is still a challenge to obtain accurate complex three-dimensional cavitating flow field. The experimental study is too expensive, and has limitations in reconstructing complex three-dimensional flow fields. While the computational fluid dynamics (CFD) is a better choice to have a deeper understanding into the flow details (Liu et al., 2019a, 2023, 2024c). Recently, combination of CFD and machine learning has shown promising potential for flow prediction and flow control (Liu et al., 2024a,b). It is well known that turbulence simulation has a significant impact on the prediction accuracy of cavitation flow. Direct numerical simulation (DNS) and large-eddy simulation (LES) are well-known high-fidelity methods, typically utilized to reveal the flow mechanism at low Reynolds number (Liu et al., 2022). The Reynolds-averaged Navier–Stokes (RANS) method is the most widely used approach in engineering, though the utilization of turbulence models for predicting complex vortical flows consistently presents an exceptional challenge (Liu et al., 2008, 2011, 2020; Li and Liu, 2022). In recent years, the hybrid RANS-LES method, combining the superiorities of RANS and LES methods, are increasingly used to predict complex flow (Liu et al., 2017; Yan et al., 2018; Fang et al., 2019; Gao and Liu, 2019; Liu et al., 2019b; Zhong et al., 2024). Although some commonly used hybrid RANS-LES methods, such as detached eddy simulation (DES) (Spalart, 2009) and scale-adaptive simulation (SAS) (Menter and Egorov, 2010), etc., usually have higher prediction accuracy, there are still some drawbacks in their application, including high grid requirement, modeled-stress depletion, etc., requiring further development. Recently, a new high-fidelity hybrid RANS-LES method, termed as the grid-adaptive simulation (GAS), was proposed (Wang and Liu, 2022). In GAS, the shear-stress transport (SST)  $k-\omega$  model is used as the baseline turbulence model, and the viscosity of SST is reasonably modified by considering the ratio of grid scale to turbulent integral length scale. The GAS method has been validated by predicting circular cylinder flow, simplified tip leakage flow and periodic hill flow. The predicted results of GAS based on coarse meshes are usually more consistent with the DNS/LES or experimental data than the results predicted by SAS and delay-DES methods, showing the potential of GAS to achieve high accuracy with low grid requirement. Moreover, its performance for predicting unsteady cavitating flow is also validated by the experimental and LES results, and shows a better accuracy than the SAS (Xie et al., 2023).

In this study, GAS is employed to investigate the unsteady cavitating flow around a NACA0009 hydrofoil with gap sizes of 1 and 10 mm, respectively. Numerical results based on a coarse mesh are firstly compared with the experimental and LES results, to validate the grid-adaptive ability and prediction accuracy. Then the evolution of cavities and vortices are systematically investigated at different gap size conditions. The multi-scale vortical structures and cavities are visualized using particle tracing method to reflect the two-layer structure of the TLV. The effects of gap size on the stability of complex flow structures are also discussed in detail.

## Methodology

### Geometry and mesh of the NACA0009 hydrofoil

According to the experiments (Dreyer et al., 2014; Dreyer, 2015), the geometry and computational domain of the NACA0009 hydrofoil are shown in Figure 1. The incidence angle is  $10^\circ$  with a chord length ( $C$ ) of 100 mm. The maximum thickness of the hydrofoil is 9.9 mm, and the thickness distribution is referred to Dreyer et al. (2014). The computational domain has a cross section of  $1.5C \times 1.5C$  and a length of  $7.5C$ . The reference length ( $L$ ) of tunnel cross section is defined as  $1.5C$ . The Cartesian coordinate system origin is located at the center of the hydrofoil root. The boundary conditions in numerical simulations are consist with experiment. The inlet is at  $2.5C$  upstream of the coordinate system origin. Inlet velocity ( $U$ ) is 10 m/s with a turbulence intensity of 1%, and inlet time-averaged pressure ( $p_\infty$ ) is kept to 1 bar. The non-slip boundary condition is applied to walls of the tunnel and hydrofoil. The gap size ( $h$ ) between the tunnel and hydrofoil tip is varied smoothly between  $0C$  and  $0.2C$  in the experiment. In this study, the cases with non-dimensional gap size ( $h/C$ ) of 0.1 and 0.01 are studied to have a deeper understanding of the effect of gap size on the evolutions of multi-scale vortical structures and cavities. In this study, the  $x$  coordinate is nondimensionalized based on  $L$ , that is, the tips of hydrofoil with small and large gap are located at  $x/L = 14.9/15$  and  $14/15$ , respectively.

More details of meshes are shown in our previous study (Xie et al., 2023). The fine mesh that contains 11.8 million cells is employed for LES case, and the medium mesh (M1) that contains 7.6 million cells is used for GAS and SAS cases. In this study, the coarse mesh (M2) containing approximately 3.8 million cells is used for GAS cases. Comparison of grid scales in refined region are shown in Figure 2. The minimum grid scales of three meshes are 0.45, 0.5 and 0.75 mm, respectively. The simulation results show that the  $y^+$  of the walls is approximately 1, which meets the requirements.

### Grid-adaptive simulation

GAS method, a new high-fidelity hybrid RANS-LES method proposed recently (Wang and Liu, 2022), is employed to investigate unsteady cavitating flow around the NACA0009 hydrofoil. The SST model is chosen as the baseline turbulence model of GAS method. The ratio of grid scale to turbulent integral length scale is introduced in GAS to modify the turbulent viscosity in SST model. The modified turbulent viscosity is defined as:

$$\nu_{fs} = \frac{a_1 D_f k_m}{\max(a_1 \omega_m, SF_2)} \quad (1)$$

where  $k_m$  and  $\omega_m$  represent the turbulent kinetic energy and specific dissipation rate in SST model, respectively,  $D_f$  is the factor to rescale the turbulent viscosity:

$$D_f = \min \left[ \left( \frac{(1 - F_{GAS}) \cdot 1.074 \cdot \Delta^* + F_{GAS} l_m}{l_m} \right)^{2/3}, 1 \right] \quad (2)$$

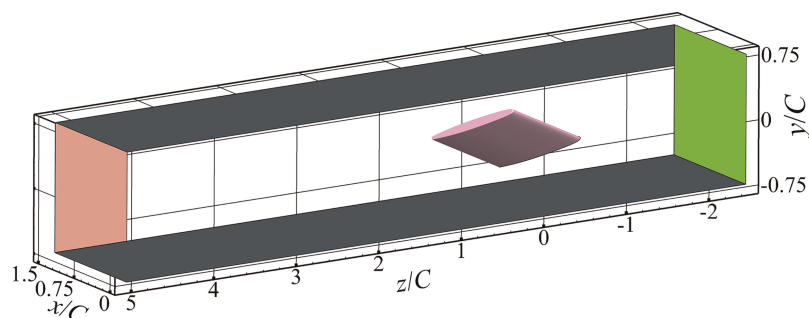


Figure 1. Geometry and computational domain of the hydrofoil.

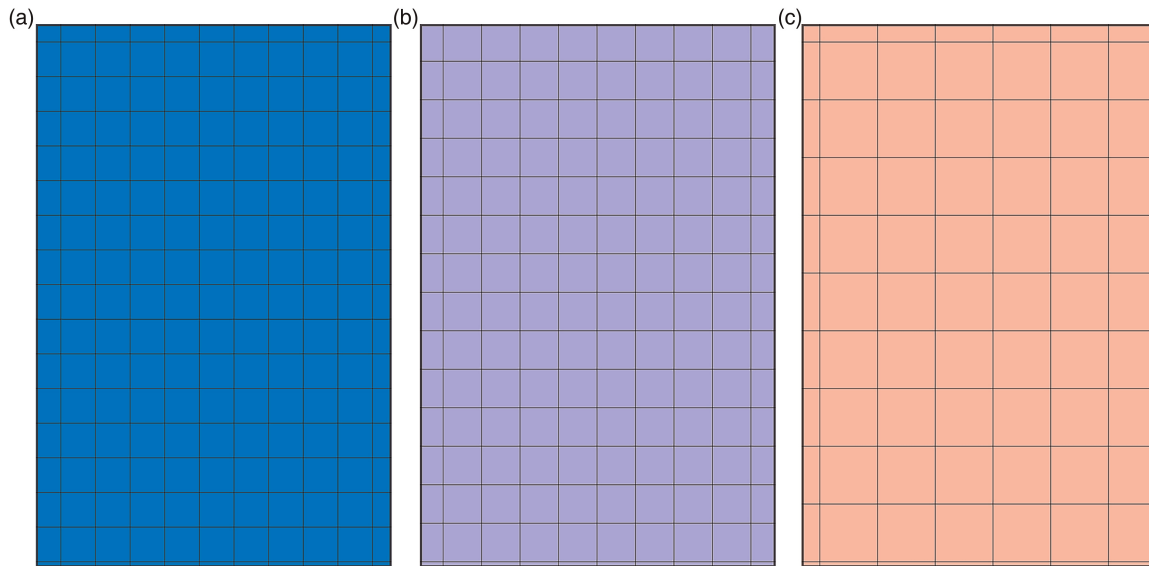


Figure 2. Comparison of grid scale in refined region. (a) LES (b) GAS M1 (c) GAS M2.

where  $l_m$  is the turbulent scale in SST model:

$$l_m = \sqrt{k_m} / (\beta^* \cdot \omega_m) \tag{3}$$

where  $\beta^* = 0.09$ , the  $F_{GAS}$  and  $\Delta^*$  are shielding function and grid scale, respectively:

$$F_{GAS} = 1 - \min[\alpha(1 - F_2), 1] \tag{4}$$

$$\alpha = \max(0.6Re_t^{0.7}, 1), Re_t = \frac{k_m}{v\omega_m} \tag{5}$$

$$\Delta^* = C_{GAS}[(1 - F_{GAS})\Delta_{vol} + F_{GAS}\Delta_{max}], C_{GAS} = 0.6 \tag{6}$$

where  $Re_t$  is the turbulent Reynolds number,  $v$  is the molecular kinematic viscosity,  $\Delta_{vol}$  represents the cube root of the grid volume, and the  $\Delta_{max}$  is the maximum grid length.

### Numerical methods

The commercial software ANSYS Fluent is employed to conduct the numerical simulations. The SIMPLEC scheme is used for pressure-velocity coupling. The second-order scheme is utilized for spatial discretization of pressure equation, and bounded central differencing scheme is applied for momentum equation. The first-order upwind scheme is utilized for the volume fraction equation. The second-order upwind scheme is utilized for turbulent kinetic energy and specific dissipation rate equations. The bounded second-order implicit scheme is applied for transient formulation. Moreover, warped-face gradient correction and high order term relaxation are also used to improve the convergence. The time step is set to  $2.5 \times 10^{-5}$  s with 20 iterations per time step. The CFL number in flow field is less than 0.5. The statistical quantities of monitoring points in complex flow structures reach statistical convergence, indicating that the simulations meet the requirements.

The mixture model is used to solve the mixture momentum equation. Zwart–Gerber–Belamri (ZGB) cavitation model (Zwart et al., 2004) is utilized to predict the process of phase change in the cavitating flow around a



NACA0009 hydrofoil. The interphase mass transfer rate in ZGB model is defined as:

$$\begin{cases} R_c = F_{\text{vap}} \frac{3\alpha_{\text{nuc}}(1 - \alpha_v)\rho_v}{R_B} \sqrt{\frac{2}{3} \frac{p_v - p}{\rho_l}}, & p \leq p_v \\ R_c = F_{\text{cond}} \frac{3\alpha_v\rho_v}{R_B} \sqrt{\frac{2}{3} \frac{p - p_v}{\rho_l}}, & p > p_v \end{cases} \quad (7)$$

where  $F_{\text{vap}} = 50$  and  $F_{\text{cond}} = 0.01$  are the empirical coefficients,  $\alpha_{\text{nuc}} = 5 \times 10^{-4}$  is the volume fraction of nucleation,  $R_B = 10^{-6}$  m is the bubble radius,  $\alpha_v$  is the vapor volume fraction,  $\rho_l = 997$  kg/m<sup>3</sup> is the water density and  $\rho_v = 0.0231$  kg/m<sup>3</sup> is the vapor density. The saturation vapor pressure ( $p_v$ ) is 3170 Pa, which corresponds to an ambient temperature of 25°C. Then the cavitation number and Reynolds number are derived:

$$\text{Re} = \frac{UC}{\nu} \approx 1.1 \times 10^6, \quad \sigma = \frac{p_\infty - p_v}{0.5\rho_l U^2} \approx 1.94 \quad (8)$$

To be clear, the methods and computational setup of LES, SAS and GAS M1 cases (Xie et al., 2023) are briefly introduced in this section. In LES, a filtering function is used to divide vortices into large- and small-scale ones. The dynamic Smagorinsky–Lilly model is utilized to model the effects of small-scale vortices, thereby overcoming the limitations associated with constant coefficients. Consequently, the Smagorinsky constant varies in time and space over a fairly wide range. SAS is proposed to resolve the turbulent spectrum in unstable flow by incorporating the von Kármán length scale into the turbulence scale equation. Introducing the von Kármán length-scale imparts an LES-like character in strongly unsteady regions. The primary distinction between SAS and the standard SST model lies in the addition of an extra source term ( $Q_{\text{SAS}}$ ) to the transport equation of  $\omega$  in SAS. Differ from the GAS M2 case, the time steps of LES, SAS, and GAS M1 cases are set to  $1 \times 10^{-5}$  s.

## Results and discussion

### Validation of GAS method

In this section, the GAS method is validated by comparing with the experimental and LES results. Moreover, as shown in Figure 2, grid scale of M2 is significantly larger than M1. Thus, M1 and M2 are used to validate the grid-adaptive ability of the GAS model. Comparisons of predicted and measured time-averaged cavities at  $h/C = 0.1$  are presented in Figure 3. A red dotted line is added to indicate the boundary of the time-averaged LEC. The LEC, TLVC and tip separation vortex cavitation (TSVC) are accurately predicted by GAS on the coarse mesh M2. The scales of these cavities in GAS M2 are agree with the experimental and LES results, indicating that GAS gives a reasonable turbulent viscosity by considering grid scale, and shows a LES-like behaviour.

Comparison of time-averaged cavities and blade surface pressure predicted by different methods are also shown in Figure 4. The SAS significantly underestimates the macroscale cavities, especially the LEC. The inception of

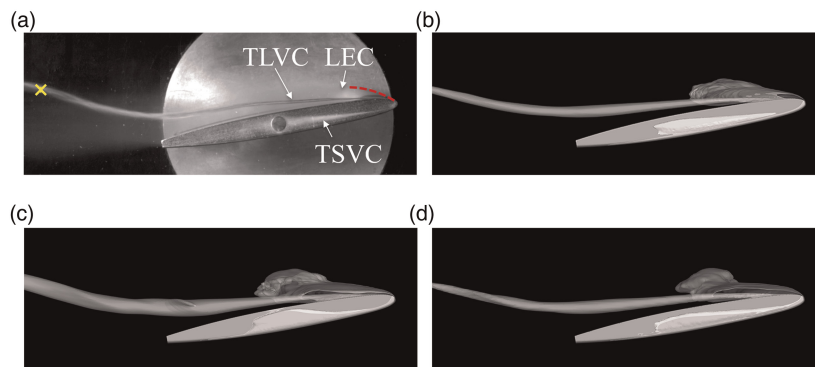


Figure 3. Predicted and measured time-averaged cavities ( $\alpha_v = 0.1$ ),  $h/C = 0.1$  (Dreyer et al., 2014). (a) EXP (b) LES, (c) GAS M1 (d) GAS M2.

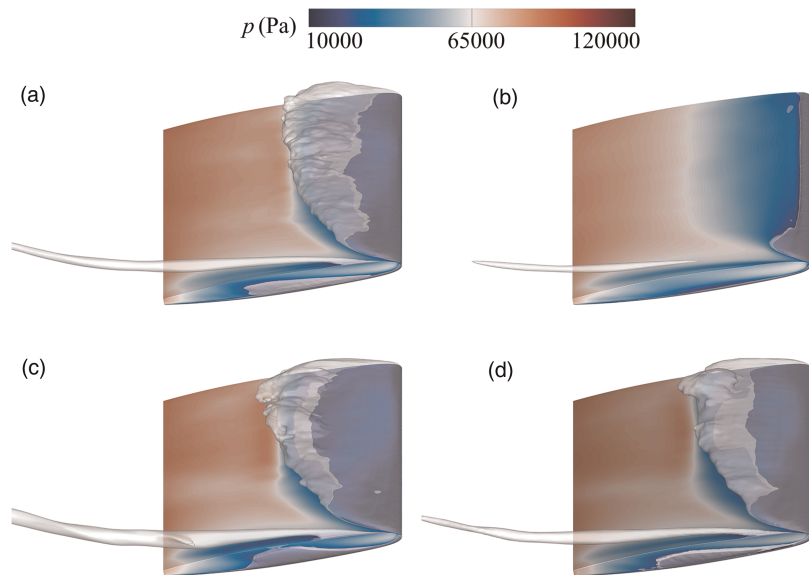


Figure 4. Comparison of time-averaged pressure and cavities ( $\alpha_v = 0.1$ ) Predicted by different methods. (a) LES, (b) SAS M1, (c) GAS M1, (d) GAS M2.

TLVC is delayed, and the cavity closure occurs more rapidly. Moreover, the SAS does not predict the occurrence of TSVC. The predicted results of GAS M2 are more consist with the LES data than the results predicted by SAS based on M1, showing the ability of GAS to achieve high accuracy with low grid requirement.

Quantitative comparisons of time-averaged streamwise velocity are shown in Figure 5. The negative streamwise velocity resulted from the re-entrant jet in LEC region is clearly captured by GAS. Both GAS M1 and GAS M2 results have good agreement with the LES data at  $x/L = 7/15$  and  $x/L = 12/15$ , indicating that the GAS method has good grid-adaptive ability. Comparison of predicted and measured cavities at  $h/C = 0.01$  are also shown in

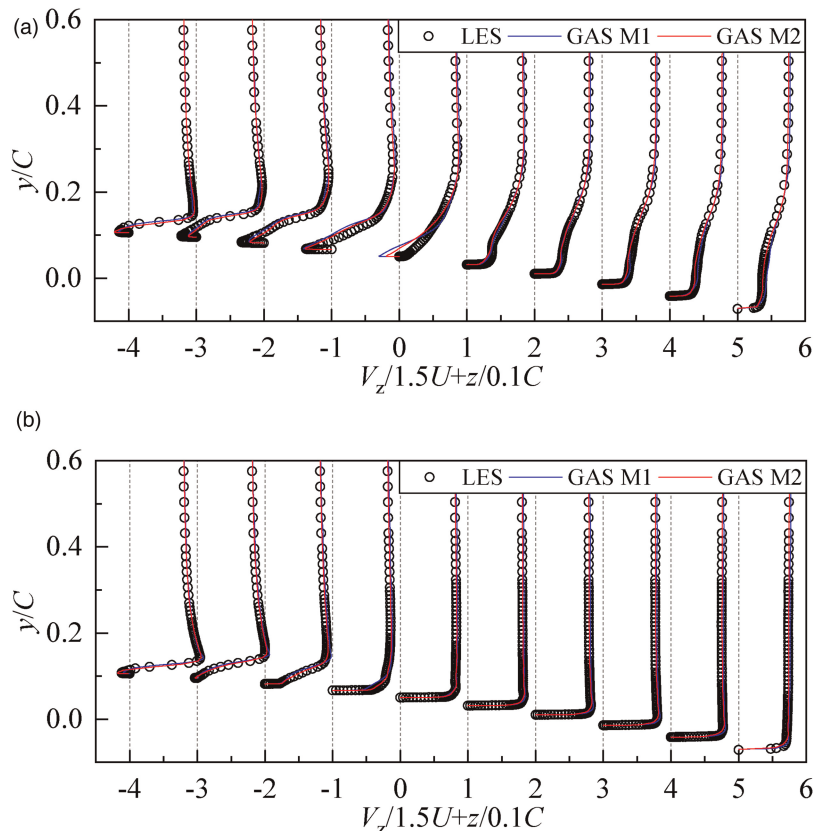


Figure 5. Comparison of time-averaged streamwise velocity,  $h/C = 0.1$  (Xie et al., 2023). (a)  $x/L = 7/15$ , (b)  $x/L = 12/15$ .

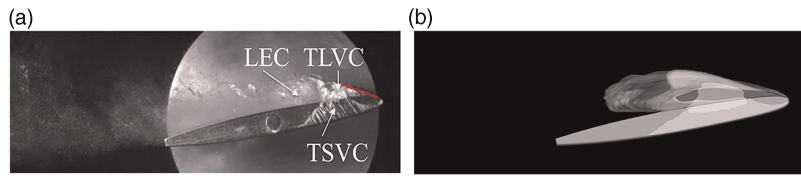


Figure 6. Predicted and measured cavities ( $\alpha_v = 0.1$ ,  $h/C = 0.01$  (Dreyer et al., 2014)). (a) EXP (b) GAS M2.

Figure 6. The key flow structures, such as LEC, TLVC, and TSVC, are clearly captured by GAS, further validating the performance of GAS. In the following sections, the results of the GAS method based on M2 are analysed in detail.

### Evolution of cavities and vortices

The local trace criterion ( $LT_{cri}$ ) (Liu and Tang, 2019; Liu et al., 2021) is used to extract multi-scale vortical structures in cavitating flow. In  $LT_{cri}$ ,  $\Psi = (\nabla \mathbf{u})^2/2$  based on the quadratic velocity gradient tensor is defined, and the value of  $LT_{cri}$  is defined as the first invariant of  $\Psi$ . The simplified form of the  $LT_{cri}$  is:

$$LT_{cri} = \begin{cases} 0 & \Delta \leq 0 \\ -\lambda_r^2/2 - \lambda_{cr}^2 + \lambda_{ci}^2 & \Delta > 0 \end{cases} \quad (9)$$

where  $\Delta$  represents the discriminant of the velocity gradient tensor (Chong et al., 1990),  $\lambda_r$  reflects the compressing or stretching rate of the spiral trajectory,  $\lambda_{cr}$  is the real part of the complex eigenvalue of the  $\nabla \mathbf{u}$ , representing the radial expansion or contraction, and  $\lambda_{ci}$  is the imaginary part of the complex eigenvalue of  $\nabla \mathbf{u}$ .

Evolution of cavities and vortical structures within a period ( $T_1$ ) are demonstrated in Figure 7. At  $h/C = 0.01$ , the development of cavities shows periodical growth and collapse. The LEC exhibits a stable sheet cavity attaching to the leading-edge (LE) at  $0/4 T_1$ , and cavity length reaches its maximum at  $2/4 T_1$ . While, the cavity is cut off rapidly, resulting in cloud cavitation shedding at  $3/4 T_1$ . LEC is the most important flow structure in small gap size unsteady cavitating flow. The lengths of the TLVC and TSVC are always smaller than that of LEC. The vortex identification results indicate that there is a significant positive correlation between the TLV breakdown and LEC development. When LEC is cut off at  $3/4 T_1$ , the TLV also becomes instability, with a concentrated vortex breaking into small vortices. It should be noted that some small-scale vortices with higher circulation in cloud cavitation shedding region also form cavities in their core. Moreover, the small gap leads to the formation of horseshoe vortex near the tip, but the cavity does not occur in the vortex core, indicating that the strength of horseshoe vortex is weak. Differ from the small gap condition, the scale of LEC is smaller, while the TLVC and TSVC are longer at  $h/C = 0.1$ . The concentrated leakage vortex develops far downstream without breaking. In addition, the horseshoe vortex upstream of the tip also disappears. Time-averaged cavities and

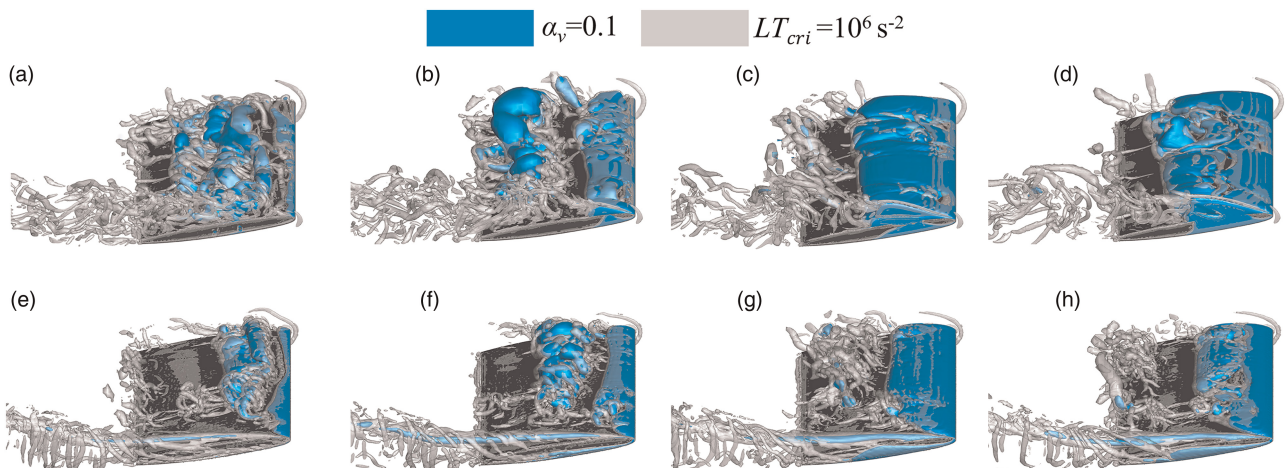


Figure 7. Evolution of cavities and vortical structures. (a)  $0/4 T_1$ ,  $h/C = 0.01$ , (b)  $1/4 T_1$ ,  $h/C = 0.01$ , (c)  $2/4 T_1$ ,  $h/C = 0.01$ , (d)  $3/4 T_1$ ,  $h/C = 0.01$ , (e)  $0/4 T_1$ ,  $h/C = 0.1$ , (f)  $1/4 T_1$ ,  $h/C = 0.1$ , (g)  $2/4 T_1$ ,  $h/C = 0.1$ , (h)  $3/4 T_1$ ,  $h/C = 0.1$ .

vortical structures are depicted in Figure 8. The trajectory of the TLV moves away from the hydrofoil as the gap size decreases. The position of induced vortex is also closely related to the gap size.

The temporal-spatial distribution of pressure coefficient at  $h/C = 0.01$  is presented in Figure 9 to further investigate the characteristics of LEC. The pressure coefficient is defined as:

$$C_p = \frac{p - p_\infty}{0.5\rho_l U^2} \tag{10}$$

The ordinate represents that the data of twenty reference times ( $T = C/U$ ) are plotted. According to the relationship between  $C_p$  and  $\sigma$ , the  $C_p$  lower than  $-1.94$  means that the LEC is attached to the hydrofoil. As shown in Figures 7 and 8, the cavitating flow at  $h/C = 0.01$  shows a quasi-two-dimensional flow; thus,  $x/L = 7/15$  is defined as the mid-span of two gap size cases. As mentioned earlier, the tips of hydrofoil with small and large gaps are located at  $x/L = 14.9/15$  and  $14/15$ , respectively. In this section, a position 2 mm below the hydrofoil tip is defined as near tip, thus the near tip positions of small and large gaps are located at  $x/L = 14.7/15$  and  $13.8/15$ , respectively.

In Figure 9(a), the growth and collapse of the cavity is observed very clearly at mid-span and near tip. At present, it is widely recognized that the large-scale LEC is cut off rapidly by the re-entrant jet with high pressure, resulting in the cloud cavitation shedding. In this study, the re-entrant jet with high pressure is shown by a red dotted line, and the cloud cavitation shedding region is presented by a white dotted line. According to the development of the re-entrant jet, it is believed that jet originates from the closure region of the LEC and flows to the LE, indicating that the cloud cavitation shedding always starts at LE. It should be noted that the velocities of re-entrant jet and cloud cavitation shedding are almost equivalent. Combining with Figure 7, the re-entrant jet is believed to have a strongly interact with the large-scale cavity. This is because the cloud cavitation shedding is induced by the smaller fragmented vortical structures with significant circulation and low pressure in their cores. Consequently, these smaller structures can sustain for a longer time until they collapse near the trailing edge

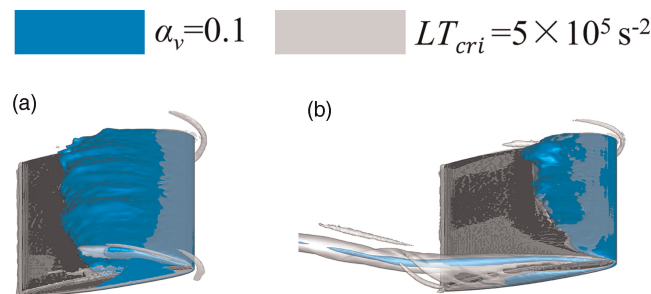


Figure 8. Time-averaged Iso-surfaces of cavities and vortical structures. (a)  $h/C = 0.01$ , (b)  $h/C = 0.1$ .

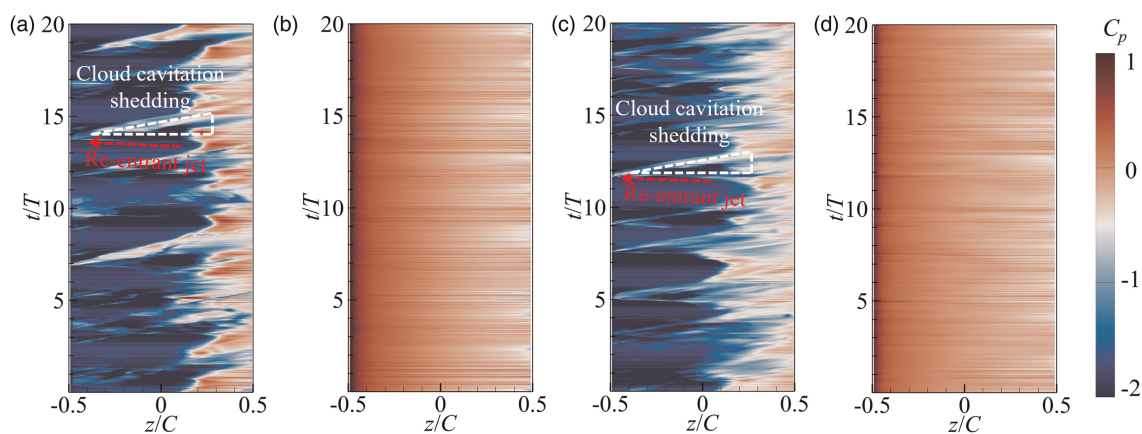


Figure 9. Temporal-spatial distributions of instantaneous pressure coefficient,  $h/C = 0.01$ . (a) SS,  $x/L = 7/15$  (b) PS,  $x/L = 7/15$  (c) SS,  $x/L = 14.7/15$  (d) PS,  $x/L = 14.7/15$ .



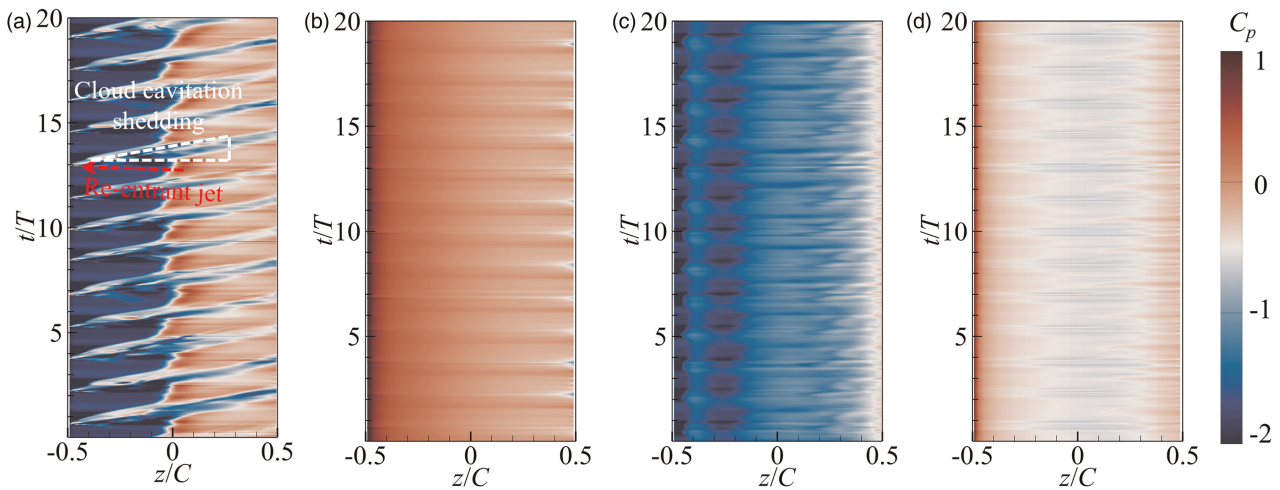


Figure 10. Temporal-spatial distributions of instantaneous pressure coefficient,  $h/C = 0.1$ . (a) SS,  $x/L = 7/15$  (b) PS,  $x/L = 7/15$  (c) SS,  $x/L = 13.8/15$  (d) PS,  $x/L = 13.8/15$ .

(TE). Another feature observed in Figure 9 is that the flow characteristics at mid-span and near tip are similar, indicating that the flow can be approximated as quasi two-dimensional at  $h/C = 0.01$ .

Temporal-spatial distributions of  $C_p$  at  $h/C = 0.1$  are shown in Figure 10. A very clear shedding frequency can be observed at mid-span [Figure 10(a)]. In addition to the characteristic frequency and cavity scale, the evolution processes of cloud cavitation shedding and re-entrant jet are basically consistent with that of small gap size. It should be noted that the flow structures near the tip is significant differently from the mid-span, exhibiting strong three-dimensional characteristics. Although the frequency of the low-pressure region on the SS of the hydrofoil tip is consistent with frequency of LEC, the cavity at LE exhibits small-scale attached cavity. There is another low-pressure region at the  $z/C = -0.25$ , and the peak value of  $C_p$  on the SS of the blade tip appears at the TE, which is also significantly different from the mid-span. The  $C_p$  on the PS of the blade tip is also lower, indicating a smaller blade load near tip at large gap size. It is noted that due to the different scales of LEC regions, the frequency of LEC  $h/C = 0.01$  is significantly lower than the frequency at  $h/C = 0.1$ .

Quantitative comparisons of time-averaged  $C_p$  on blade surface are shown in Figure 11. The difference of  $C_p$  on the PS at mid-span between two gap sizes is negligible. The length of low  $C_p$  region is consistent with that of the time-averaged cavities. Moreover, due to the large scale of the cavities at  $h/C = 0.01$ , the distance between the cavities and the hydrofoil is smaller. Consequently, the  $C_p$  of time-averaged cavities at  $h/C = 0.01$  is still lower than that of the large gap size case. Furthermore, the closure position of the LEC is stable at  $h/C = 0.1$  due to its periodicity, thus the slope of  $C_p$  at closure position is large. However, in the case of small gap size, there is no obvious dominant frequency, so the slope of  $C_p$  is relatively lower. The difference of  $C_p$  near the tip for different gap sizes is more significant. The fluid near the PS of hydrofoil is affected by the unloading of the blade gap,

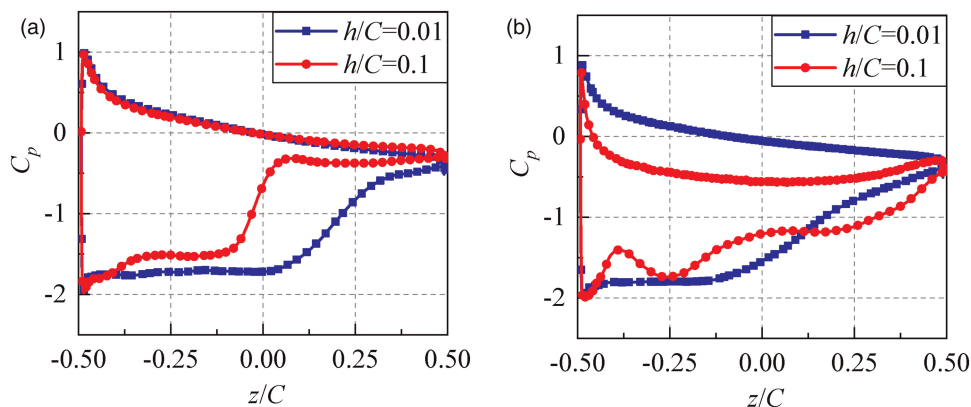


Figure 11. Distribution of time-averaged pressure coefficient. (a)  $x/L = 7/15$  (b)  $x/L = 14.7/15$  at  $h/C = 0.01$ ,  $x/L = 13.8/15$  at  $h/C = 0.1$ .



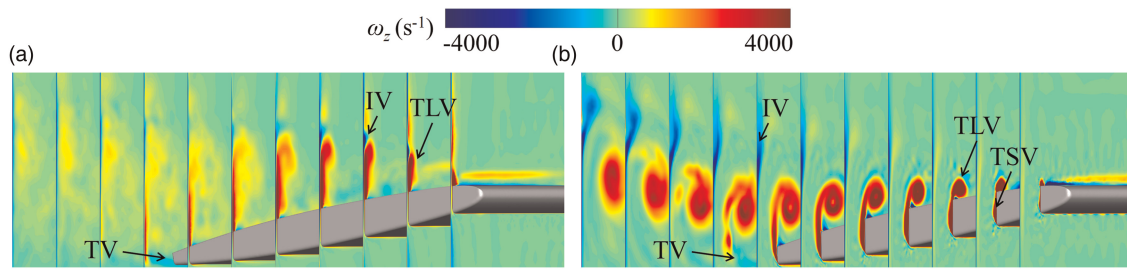


Figure 12. Distribution of time-averaged streamwise vorticity. (a)  $h/C = 0.01$ , (b)  $h/C = 0.1$ .

and this effect is positively related to the gap size, so the  $C_p$  on the PS is significantly smaller at  $h/C = 0.1$ . As shown in Figures 7 and 8, the local minimum  $C_p$  at  $z/C = -0.25$  is induced by the TLVC.

### Effect of gap size on the flow structures evolution

As described above, the gap size has a significant impact on the evolution of cavities and vortical structures. Further research is needed on the interactions of these structures need. Figures 12 and 13 depict the distributions of time-averaged streamwise vorticity and pitchwise velocity. It is found that the TLV at  $h/C = 0.1$  has a larger scale and higher vorticity, while the overall vorticity of TLV at  $h/C = 0.01$  is relatively small. It is noted that the IV at  $h/C = 0.01$  is closer to the upstream. The distribution of radial velocity indicates that the jet velocity is higher near the LE, resulting in local strong TLV and IV near LE. The higher jet velocity also leads to a purely potential effect, namely elevation of the TLV trajectory. Moreover, the tunnel wall also has an effect on nearby TLV, which can be explained by image vortex, further promoting the elevation of the TLV. However, a smaller gap means less leakage flow, affecting the vorticity transport from the tip to the TLV. Thus, the strength of the TLV decreases rapidly under the effect of the boundary layer of the tunnel wall. As shown in Figure 12(b), the TSV begin to merge with TLV at half chord position. The vorticity of TLV further increases due to the supply of tip leakage flow, resulting in the appearance of IV. While the TSV is negligible under the suppression effect of the jet at  $h/C = 0.01$ . Furthermore, the streamwise vorticity in the TLVC region at  $h/C = 0.1$  is smaller than that of the vapor-liquid interface, it is on account of the expansion of cavities. Thus, the vorticity of the TLV core is transported to the vapor-liquid interface (Xie et al., 2023).

In this section, the multi-scale vortical structures and cavities are also visualized using particle tracing method to understand the flow mechanism. A streakline is a snapshot of all the particles that passed through a particular Eulerian point in the flow field. In this investigation, the streaklines are extracted by continuously releasing fluid particles at the same position and recording the locations of these particles at a set of instants. The seeding points are placed in cavities and vortical structures to capture their flow features, as shown in Figure 14. The seeding points along the TLV core are used to visualize the wandering of the TLV. The seeding points upstream of the LE are employed to exhibit the evolution of LEC, as well as the interaction between the LEC and the TLVC. The seeding points in the gap are utilized to reflect the interaction between the TSVC and the TLVC. The seeding points downstream of the TE is used to reflect the impact of the trailing-edge vortex (TEV) on the stability of the TLV. The seeding points are released by the same time interval  $T/100$ . Then the positions of fluid particles are calculated using fourth-order Runge–Kutta integration.

The snapshots of streaklines of flow structures are presented in Figure 15. The fluid particles are colored by instantaneous streamwise velocity. In our previous studies (Hou et al., 2022; Hou and Liu, 2023), the TLV is

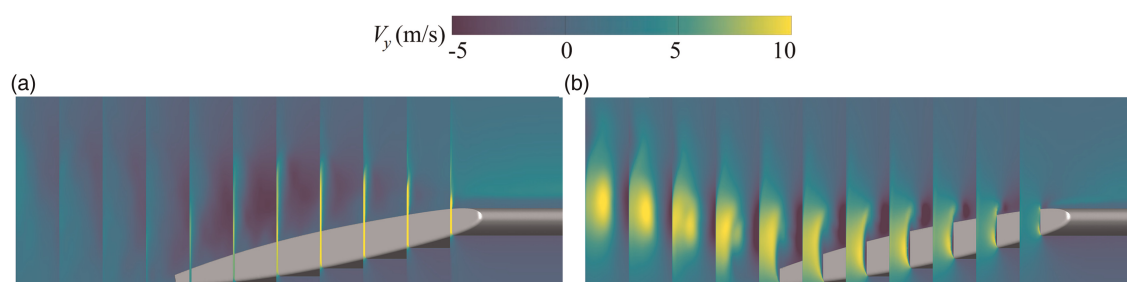


Figure 13. Distribution of time-averaged pitchwise velocity. (a)  $h/C = 0.01$ , (b)  $h/C = 0.1$ .

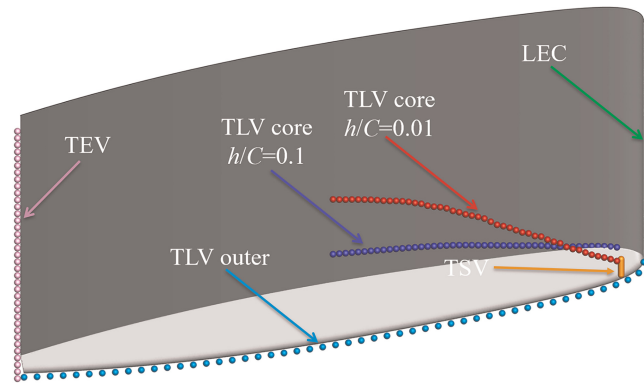


Figure 14. Locations of seeding points.

composed of a two-layer structure, so two sets of seeding points are set in the TLV core and gap. The fluid particles in LEC clearly demonstrate the periodic process of cloud cavitation shedding and re-entrant jet. As shown in Figures 15(c)–15(f), the velocities of fluid particles in the TLV core and outer layer are similar, regardless of the gap size. Only in the generation stage of the TLV, the streamwise velocity of the TLV is relatively high at  $h/C = 0.01$ . As discussed before, the losses arising from the tunnel boundary layer is the main factor results in a streamwise velocity deficit in the TLV. This conclusion is consistent with the previous results (Batchelor, 1964). Further, the fluid particles in the TLV at  $h/C = 0.01$  exhibit low-frequency fluctuation due to the effect of LEC periodical development, which may also suppress the vorticity transport related to the TLV. Unlike the TLV that

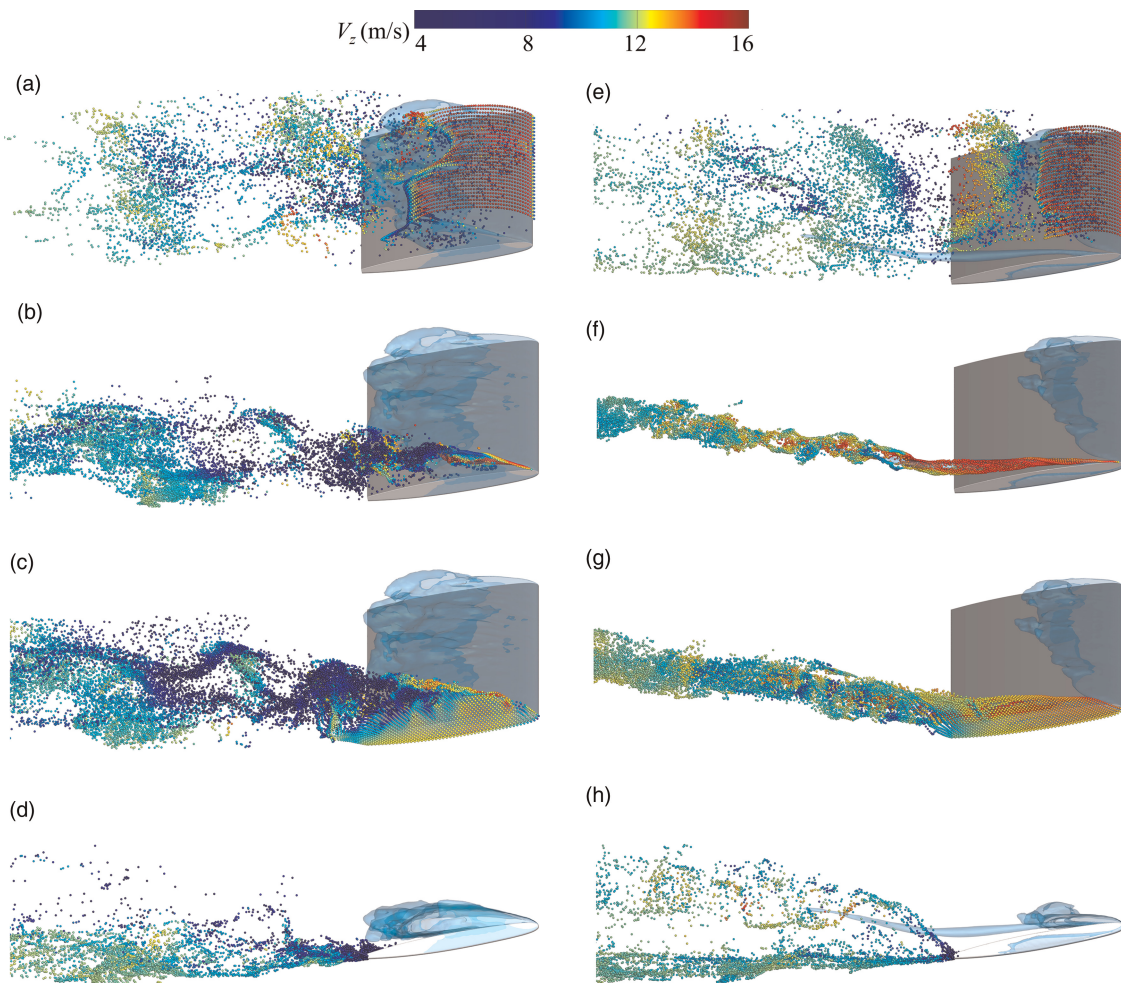


Figure 15. Snapshots of streaklines of flow structures. (a) LEC,  $h/C = 0.01$ , (b) LEC,  $h/C = 0.1$ , (c) TLV core,  $h/C = 0.01$ , (d) TLV core,  $h/C = 0.1$ , (e) TLV outer,  $h/C = 0.01$ , (f) TLV outer,  $h/C = 0.1$ , (g) TEV,  $h/C = 0.01$ , (h) TEV,  $h/C = 0.1$ .

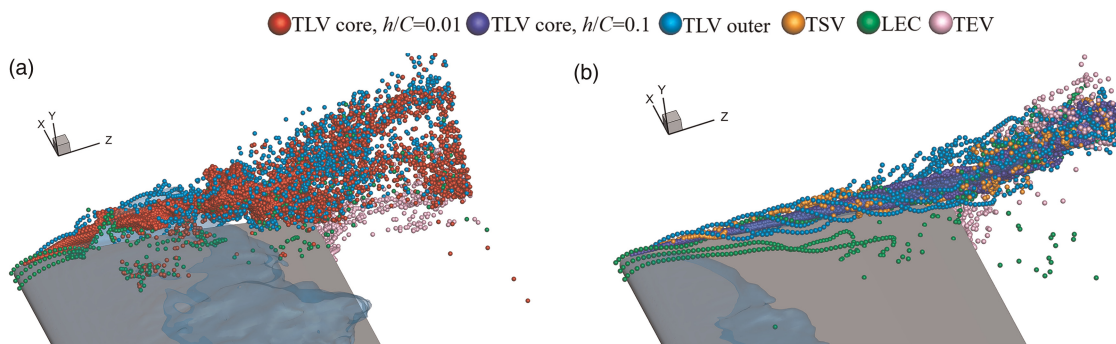


Figure 16. Summary of streaklines of complex flow structures. (a)  $h/C = 0.01$ . (b)  $h/C = 0.1$ .

become instability and breaks prematurely at  $h/C = 0.01$ , the TLV at  $h/C = 0.1$  is more stable from LE to TE, and shows a jet-like behavior. However, at the downstream of hydrofoil, the TLV at  $h/C = 0.1$  also exhibits slightly instability. Figures 15(g) and 15(h) reflect the influence of TEV on the stability of TLV. It is clearly observed that due to a small distance between the TLV and hydrofoil, the TEV near the gap is captured by TLV at  $h/C = 0.1$ . However, the vorticity transport process between the TEV and TLV is weak at  $h/C = 0.01$ . It is also found that a portion of the wake flows back to the SS of the hydrofoil, which results from the periodic evolution of large-scale LEC.

All the streaklines of complex flow structures are shown in Figure 16. The fluid particles are colored by their release position, according to Figure 12. At small gap size condition, the vorticity transport from tip to the TLV is weak, resulting in an indistinct two-layer structure of the TLV. As the TLV develops, the fluid particles released from the TLV core, TLV outer layer, and LEC are mixed. The particles of the wake are basically located at the bottom of the TLV. As the gap size increases, the two-layer structure of TLV becomes significant. The inner TLV core region is generated by the vorticity transport from the tip to the TLV. The TLV core region corresponds to TLVC, in which no particles released from other structures appears. The structure of the outer layer including the mainstream, TSV and leakage flow, is formed by the shearing between the tip leakage flow and the passage flow. The complex outer layer plays a crucial role in affecting the stability of TLV as well as cavities.

The investigation on TLV structure in this study of cavitation flow is in good agreement with the previous conclusions in compressors (Hou et al., 2022), indicating that two-layer structure of the TLV is a universal phenomenon, providing support for the mechanism research and flow control of the TLVC in the future.

## Conclusions

In this study, numerical investigation of unsteady cavitating flow around a NACA0009 hydrofoil with gap sizes of 1 and 10 mm is conducted using GAS method. Firstly, the performance of GAS is validated. A detailed study on the effect of gap size with an emphasis on the evolution of complex vortical structures is also performed. The main conclusions are summarized as follows:

1. The GAS method is validated by comparing with experimental and LES results. The complex flow structures are accurately predicted by GAS, and the scales of these structures are consistent with the experimental and LES results, indicating that GAS gives a reasonable turbulent viscosity and shows a LES-like behaviour. The results of GAS based on mesh with different grid scales are in good agreement with the LES data, reflecting that the GAS method has satisfactory grid-adaptive ability.
2. Evolution of cavities and vortices are systematically investigated at different gap sizes. Temporal-spatial distributions of instantaneous pressure coefficient show clearly the growth and collapse of the cavity. The flow characteristics at mid-span and near tip are similar, indicating that the flow can be approximated as quasi two-dimensional at small gap condition. However, a very clear shedding frequency is observed at large gap, and the flow exhibits strong three-dimensional characteristics. The cloud cavitation shedding always starts at leading edge, regardless of the gap size. The re-entrant jet is found to have a strongly interact with the large-scale cloud cavity.
3. The multi-scale vortical structures and cavities are visualized using particle tracing method. As the gap size increases, the two-layer structure of the TLV becomes clear. The inner TLV core region is generated by the vorticity transport from the tip to the TLV. The structure of the outer layer is formed by the shearing between the leakage flow and the mainstream. The complex outer layer plays a crucial role in affecting the

stability of the TLV and cavities. The investigation on the TLV structure of cavitation flow is in good agreement with the previous conclusions in compressors, indicating that two-layer structure of TLV is a universal phenomenon.

## Nomenclature

LES	large-eddy simulation
GAS	grid-adaptive simulation
TLV	tip leakage vortex
TLVC	tip leakage vortex cavitation
TSV	tip separation vortex
TSVC	tip separation vortex cavitation
TEV	trailing-edge vortex
LEC	leading-edge cavitation
TSVC	tip separation vortex cavitation
SS	suction side
PS	pressure side
$L$	reference length of tunnel (m)
$U$	inlet velocity (m/s)
$C$	chord length (m)
$T$	reference time $c/u$ (s)
$T_1$	cavities evolution period (s)
$LT_{cri}$	local trace criterion ( $s^{-2}$ )
$\alpha_v$	vapor volume fraction
$\rho$	density ( $kg/m^3$ )
Re	Reynolds number
$\sigma$	cavitation number

## Funding sources

This work is supported by the National Natural Science Foundation of China (51976006, 52106039), the Industry-University-Research Cooperation Project of AECC (HFZL2022CXY001, HFZL2023CXY002), and the Fundamental Research Funds for the Central Universities.

## Competing interests

Nan Xie declares that he has no conflict of interest. Yumeng Tang declares that she has no conflict of interest. Jiexuan Hou declares that she has no conflict of interest. Yangwei Liu declares that he has no conflict of interest.

## References

- Batchelor G. K. (1964). Axial flow in trailing line vortices. *Journal of Fluid Mechanics*. 20 (4): 645–658. <https://doi.org/10.1017/S0022112064001446>.
- Boulon O., Callenaere M., Franc J.-P., and Michel J.-M. (1999). An experimental insight into the effect of confinement on tip vortex cavitation of an elliptical hydrofoil. *Journal of Fluid Mechanics*. 390: 1–23. <https://doi.org/10.1017/S002211209900525X>.
- Chong M. S., Perry A. E., and Cantwell B. J. (1990). A general classification of three-dimensional flow fields. *Physics of Fluids A: Fluid Dynamics*. 2 (5): 765–777. <https://doi.org/10.1063/1.857730>.
- Dreyer M. (2015). Mind the gap: Tip leakage vortex dynamics and cavitation in axial turbines. Ph.D. École Polytechnique Fédérale de Lausanne.
- Dreyer M., Decaix J., Münch-Alligné C., and Farhat M. (2014). Mind the gap: a new insight into the tip leakage vortex using stereo-PIV. *Experiments in Fluids*. 55: 1849. <https://doi.org/10.1007/s00348-014-1849-7>.
- Fang J., Gao Y., Liu Y., Lu L., Yao Y., and Le Ribault C. (2019). Direct numerical simulation of a tip-leakage flow in a planar duct with a longitudinal slit. *Physics of Fluids*. 31 (12): 125108. <https://doi.org/10.1063/1.5124163>.
- Farrell K. and Billet M. (1994). A correlation of leakage vortex cavitation in axial flow pumps. *ASME Journal of Fluids Engineering*. 116 (3): 551–557. <https://doi.org/10.1115/1.2910312>.
- Gao Y. and Liu Y. (2019). A flow model for tip leakage flow in turbomachinery using a square duct with a longitudinal slit. *Aerospace Science and Technology*. 95: 105460. <https://doi.org/10.1016/j.ast.2019.105460>.
- Gopalan S., Katz J., and Liu H. (2002). Effect of gap size on tip leakage cavitation inception, associated noise and flow structure. *ASME Journal of Fluids Engineering*. 124 (4): 994–1004. <https://doi.org/10.1115/1.1514496>.



- Hou J. and Liu Y. (2023). Evolution of unsteady vortex structures in the tip region of an axial compressor rotor. *Physics of Fluids*. 35 (4): 045107. <https://doi.org/10.1063/5.0141818>.
- Hou J., Liu Y., Zhong L., Zhong W., and Tang Y. (2022). Effect of vorticity transport on flow structure in the tip region of axial compressors. *Physics of Fluids*. 34 (5): 055102. <https://doi.org/10.1063/5.0087833>.
- Huang B., Qiu S., Li X., Wu Q., and Wang G. (2019). A review of transient flow structure and unsteady mechanism of cavitating flow. *Journal of Hydrodynamics*. 31 (3): 429–444. <https://doi.org/10.1007/s42241-019-0050-0>.
- Li W. and Liu Y. (2022). Numerical investigation of corner separation flow using Spalart-Allmaras model with various modifications. *Aerospace Science and Technology*. 127: 107682. <https://doi.org/10.1016/j.ast.2022.107682>.
- Liu Y. and Tang Y. (2019). An elliptical region method for identifying a vortex with indications of its compressibility and swirling pattern. *Aerospace Science and Technology*. 95: 105448. <https://doi.org/10.1016/j.ast.2019.105448>.
- Liu Y., Yu X., and Liu B. (2008). Turbulence models assessment for large-scale tip vortices in an axial compressor rotor. *AIAA Journal of Propulsion and Power*. 24 (1): 15–25. <https://doi.org/10.2514/1.26134>.
- Liu Y., Lu L., Fang L., and Gao F. (2011). Modification of Spalart-Allmaras model with consideration of turbulence energy backscatter using velocity helicity. *Physics Letters A*. 375 (24): 2377–2381. <https://doi.org/10.1016/j.physleta.2011.05.023>.
- Liu Y., Yan H., Lu L., and Li Q. (2017). Investigation of vortical structures and turbulence characteristics in corner separation in a linear compressor cascade using DDES. *ASME Journal of Fluids Engineering*. 139 (2): 021107. <https://doi.org/10.1115/1.4034871>.
- Liu Y., Tang Y., Liu B., and Lu L. (2019a). An exponential decay model for the deterministic correlations in axial compressor. *ASME Journal of Turbomachinery*. 141 (2): 021005. <https://doi.org/10.1115/1.4041380>.
- Liu Y., Zhong L., and Lu L. (2019b). Comparison of DDES and URANS for unsteady tip leakage flow in an axial compressor rotor. *ASME Journal of Fluids Engineering*. 141 (12): 121405. <https://doi.org/10.1115/1.4043774>.
- Liu Y., Tang Y., Scillitoe A. D., and Tucker P. G. (2020). Modification of shear stress transport turbulence model using helicity for predicting corner separation flow in a linear compressor cascade. *ASME Journal of Turbomachinery*. 142 (2): 021004. <https://doi.org/10.1115/1.4045658>.
- Liu Y., Zhong W., and Tang Y. (2021). On the relationships between different vortex identification methods based on local trace criterion. *Physics of Fluids*. 33 (10): 105116. <https://doi.org/10.1063/5.0063326>.
- Liu Y., Xie N., Tang Y., and Zhang Y. (2022). Investigation of hemocompatibility and vortical structures for a centrifugal blood pump based on large-eddy simulation. *Physics of Fluids*. 34 (11): 115111. <https://doi.org/10.1063/5.0117492>.
- Liu Y., Wei X., and Tang Y. (2023). Investigation of unsteady rotor-stator interaction and deterministic correlation analysis in a transonic compressor stage. *ASME Journal of Turbomachinery*. 145 (7): 071004. <https://doi.org/10.1115/1.4056716>.
- Liu Y., Zhao S., Wang F., and Tang Y. (2024a). A novel method for predicting fluid–structure interaction with large deformation based on masked deep neural network. *Physics of Fluids*. 36 (2): 027103. <https://doi.org/10.1063/5.0183290>.
- Liu Y., Wang F., Zhao S., and Tang Y. (2024b). A novel framework for predicting active flow control by combining deep reinforcement learning and masked deep neural network. *Physics of Fluids*. 36 (3): 037112. <https://doi.org/10.1063/5.0194264>.
- Liu Y., Luo P., and Tang Y. (2024c). Improved prediction of turbomachinery flows using Reynolds stress model with  $\gamma$  transition model. *Aerospace Science and Technology*. 144: 108812. <https://doi.org/10.1016/j.ast.2023.108812>.
- Menter F. R. and Egorov Y. (2010). The scale-adaptive simulation method for unsteady turbulent flow predictions. Part 1: theory and model description. *Flow, Turbulence and Combustion*. 85: 113–138. <https://doi.org/10.1007/s10494-010-9264-5>.
- Peng X., Zhang L., Wang B., Xu L., Song M., et al. (2019). Study of tip vortex cavitation inception and vortex singing. *Journal of Hydrodynamics*. 31 (6): 1170–1177. <https://doi.org/10.1007/s42241-019-0091-4>.
- Sakulkaew S., Tan C. S., Donahoe E., Cornelius C., and Montgomery M. (2013). Compressor efficiency variation with rotor tip gap from vanishing to large clearance. *ASME Journal of Turbomachinery*. 135 (3): 031030. <https://doi.org/10.1115/1.4007547>.
- Spalart P. R. (2009). Detached-eddy simulation. *Annual Review of Fluid Mechanics*. 41: 181–202. <https://doi.org/10.1146/annurev.fluid.010908.165130>.
- Wang G. and Liu Y. (2022). A grid-adaptive simulation model for turbulent flow predictions. *Physics of Fluids*. 34 (7): 075125. <https://doi.org/10.1063/5.0090485>.
- Wang X., Bai X., Cheng H., Ji B., and Peng X. (2023). Numerical investigation of how gap size influences tip leakage vortex cavitation inception using a Eulerian–Lagrangian method. *Physics of Fluids*. 35 (1): 012113. <https://doi.org/10.1063/5.0131813>.
- Williams R., Gregory-Smith D., He L., and Ingram G. (2010). Experiments and computations on large tip clearance effects in a linear cascade. *ASME Journal of Turbomachinery*. 132 (4): 021018. <https://doi.org/10.1115/1.3104611>.
- Xie N., Tang Y., and Liu Y. (2023). High-fidelity numerical simulation of unsteady cavitating flow around a hydrofoil. *Journal of Hydrodynamics*. 35 (1): 1–16. <https://doi.org/10.1007/s42241-023-0014-2>.
- Xu M., Cheng H., Ji B., and Peng X. (2020). LES of tip-leakage cavitating flow with special emphasis on different tip clearance sizes by a new Euler-Lagrangian cavitation model. *Ocean Engineering*. 213: 107661. <https://doi.org/10.1016/j.oceaneng.2020.107661>.
- Yan H., Liu Y., Li Q., and Lu L. (2018). Turbulence characteristics in corner separation in a highly loaded linear compressor cascade. *Aerospace Science and Technology*. 75: 139–154. <https://doi.org/10.1016/j.ast.2018.01.015>.
- Zhang L., Zhang N., Peng X., Wang B., and Shao X. (2015). A review of studies of mechanism and prediction of tip vortex cavitation inception. *Journal of Hydrodynamics*. 27 (4): 488–495. [https://doi.org/10.1016/S1001-6058\(15\)60508-X](https://doi.org/10.1016/S1001-6058(15)60508-X).
- Zhong W., Liu Y., and Tang Y. (2024). Unsteady flow structure of corner separation in a highly loaded compressor cascade. *ASME Journal of Turbomachinery*. 146 (3): 031003. <https://doi.org/10.1115/1.4063926>.
- Zwart P. J., Gerber A. G., and Belamri T. (2004). A two-phase flow model for predicting cavitation dynamics. In *ICMF 2004 International Conference on Multiphase Flow*, p. 152.